

Supporting Information

Highly dispersed Fe-Ru dual cocatalyst derived from Prussian blue analogue for boosting O₂ evolution on an oxyiodide photocatalyst

Reiya Takahashi,^a Hajime Suzuki,^{a,*} Harutaka Ninomiya,^a Makoto Ogawa,^a Osamu Tomita,^a Akinobu Nakada,^a Shunsuke Nozawa,^b Akinori Saeki,^c Ryu Abe^{a,*}

^a Department of Energy and Hydrocarbon Chemistry, Graduate School of Engineering, Kyoto University, Katsura, Nishikyo-ku, Kyoto 615-8510, Japan

^b Photon Factory (PF), Institute of Materials Structure Science (IMSS), High Energy Accelerator Research Organization (KEK), Tsukuba, Ibaraki 305-0801, Japan

^c Department of Applied Chemistry, Graduate School of Engineering, Osaka University, Suita, Osaka 565-0871, Japan

AUTHOR INFORMATION

Corresponding Author

* suzuki.hajime.7x@kyoto-u.ac.jp (H. S.)

* ryu-abe@scl.kyoto-u.ac.jp (R. A.)

Experimental

Materials

Bi₂O₃ (99.99%), BaCO₃ (99.99%), Nb₂O₅ (99.9%), CsI (99.9%), KI (99.9%), Bi(NO₃)₃·5H₂O (99.9%), ethanol (99.5%), SrCO₃ (99.99%), TiO₂ (Rutile, 99.0%), FeCl₃·6H₂O (99.9%), RuCl₃·*n*H₂O (≥85.0%), acetone (99.5%), Na₂SO₄ (≥99.0%), Fe(NO₃)₃·9H₂O (99.0%), and Fe(ClO₄)₃·*n*H₂O (≥70.0%) were purchased from FUJIFILM Wako Pure Chemical Corporation. Rh₂O₃ (99.9%) was purchased from Kanto Chemical Corporation. K₄[Ru(CN)₆]·*x*H₂O (98%), Ru(III) acetylacetonate (Ru(acac)₃) (97%), Fe(III) acetylacetonate (Fe(acac)₃) (97%), and Fe(ClO₄)₂·*n*H₂O (98%) were purchased from Sigma-Aldrich Co. LLC. All chemicals were used as received without further purification.

Synthesis

Ba₂Bi₃Nb₂O₁₁ was synthesized via the flux method.⁵¹ A stoichiometric mixture of Bi₂O₃, BaCO₃, Nb₂O₅, and BiOI was combined with a flux (the eutectic mixture of CsI and KI in the ratio 61:39) at a solute concentration of 5 mol% (i.e., Ba₂Bi₃Nb₂O₁₁/(Ba₂Bi₃Nb₂O₁₁ + flux)). The mixture was heated in an evacuated quartz tube to 800 °C at a heating rate of 20 °C h⁻¹ and maintained at this temperature for 20 h. After natural cooling, the product was thoroughly washed with 500 mL of distilled water, collected by vacuum filtration, and air-dried. BiOI was synthesized via a soft liquid deposition method.⁵² Specifically, 5 mmol of Bi(NO₃)₃·5H₂O was dispersed in 30 mL of ethanol and mixed with a solution of 5 mmol of KI dissolved in 10 mL of pure water. The mixture was stirred at room temperature for 5 h utilizing a magnetic stirrer bar; subsequently, the precipitate was collected by centrifugation (4800 rpm, 3 min), washed several times with water and ethanol, and dried in air at 80 °C.

SrTiO₃:Rh was synthesized via SSR.⁵³ A stoichiometric mixture of SrCO₃, TiO₂, and Rh₂O₃ (Sr/Ti/Rh = 1.07:1:0.01) was calcined in air at 800 °C for 1 h, and subsequently at 1000 °C for 10 h. A ruthenium-based cocatalyst (RuO_{*x*}; 0.7 wt% calculated as metal) was loaded onto SrTiO₃:Rh via photodeposition, employing RuCl₃·*n*H₂O as the precursor.⁵⁴

Nanoparticles of KFe[Ru(CN)₆] (hereafter denoted as FeHCRu) were prepared via a coprecipitation method.⁵⁵ 1.5 mL of aqueous Fe(NO₃)₃ solution (1 M) was added into 3 mL of aqueous K₄[Ru(CN)₆] solution (0.5 M). The mixture was vigorously stirred for 5 min. The resulting precipitate was centrifuged, washed thoroughly three times with Milli-Q water and once with methanol, and dried in an oven under vacuum for 12 h.

Loading of Cocatalysts

Iron-ruthenium cocatalyst was loaded onto photocatalyst particles via the impregnation method. For iron-ruthenium oxide ((Fe,Ru)O_{*x*}) loading, a small amount of photocatalyst was mixed with an acetone solution of Fe(acac)₃ and Ru(acac)₃ (10 mol% as Fe and Ru for Ba₂Bi₃Nb₂O₁₁), followed by heating under an Ar flow (20 mL min⁻¹) at 450 °C for 30 min.⁵¹ The resulting sample is hereafter referred to as Ba₂Bi₃Nb₂O₁₁ (acac-450 °C). For FeHCRu-derived cocatalyst loading, a small amount of photocatalyst was mixed with an aqueous suspension of FeHCRu (10 mol% as Fe and Ru for Ba₂Bi₃Nb₂O₁₁), followed by heating under an Ar flow (20 mL min⁻¹) at 100–550 °C for 30 min. The resulting samples are hereafter referred to as Ba₂Bi₃Nb₂O₁₁ (FeHCRu-*T* °C).

Characterization

Powder X-ray diffraction (XRD; MiniFlex600-C, Rigaku, X-ray source: Cu K α), UV-visible diffuse reflectance spectroscopy (V-650, JASCO), scanning electron microscopy (SEM; NVision 40, Carl Zeiss-SIINT) equipped with energy-dispersive X-ray spectroscopy (EDX), attenuated total reflectance-Fourier transform infrared spectroscopy (ATR-FTIR; FT/IR-4200, JASCO), and X-ray photoelectron spectroscopy (XPS; JPS-9200, JEOL, X-ray source: Mg K α) were employed for sample characterization. The XPS binding energies were calibrated using the 4f_{7/2} peak of Au (83.3 eV) deposited on the sample surface. Thermogravimetric and differential thermal analysis (TG-DTA; Thermo plus EVO2, Rigaku) was performed at the heating rate of 10 °C min⁻¹ up to 1000 °C under N₂ flow (100 mL min⁻¹). Annular dark-field scanning transmission electron microscopy (ADF-STEM) images were collected utilizing JEM-ARM200CF operating at an accelerating voltage of 120 kV. Elemental analysis was performed employing JEM-ARM200CF equipped with an EDX spectroscopy system. Transmission electron microscopy (TEM) images were collected utilizing JEM-2200FS operating at an accelerating voltage of 200 kV. Fe K-edge and Ru K-edge X-ray absorption fine structure (XAFS) spectra were collected in transmission

or fluorescence mode at beamlines BL12C and NW10A of the Photon Factory (PF) and Photon Factory Advanced Ring (PF-AR) at the High Energy Accelerator Research Organization (KEK).

Time-Resolved Microwave Conductivity (TRMC) Measurements

TRMC measurements were performed in an ambient atmosphere at room temperature (25 °C). The third harmonic generation (THG; 355 nm) of a Nd:YAG laser (Continuum Inc., Surelite II, 5–8 ns pulse duration, 10 Hz) was used as the excitation source, and an X-band microwave (~9.1 GHz) was used as the probe. The powdered samples were affixed to quartz substrates using optically clear adhesive tape, ensuring that the tape did not interfere with the TRMC signal. The photoconductivity $\Delta\sigma$ was calculated using the following formula: $\Delta\sigma = \Delta P_r / (AP_r)$, where ΔP_r , A , and P_r are the transient power change of the reflected microwave, sensitivity factor, and power of the reflected microwave, respectively. The obtained $\Delta\sigma$ values were then converted to the product of the quantum yield (φ) and the sum of the charge carrier mobilities ($\Sigma\mu = \mu_+ + \mu_-$) using the following formula: $\varphi\Sigma\mu = \Delta\sigma(eI_0F_{\text{light}})^{-1}$, where e , I_0 , and F_{light} are the unit charge of a single electron, incident photon density of the excitation laser, and a correction (or filling) factor, respectively. The fitting of TRMC transients was conducted using a stretched exponential function: $\alpha \exp(-(kt)^\beta)$, where α , k , and β are the coefficient, rate constant, and power factor of the exponent, respectively. The value of β was fixed at 0.20 to ensure consistency in the comparison of the decays. The lifetime (τ) was defined as the inverse of k ($\tau = 1/k$). The TRMC signal of $\text{Ba}_2\text{Bi}_3\text{Nb}_2\text{O}_{11}\text{I}$ is mainly derived from photogenerated electrons since $\text{Ba}_2\text{Bi}_3\text{Nb}_2\text{O}_{11}\text{I}$ shows an n-type semiconducting characteristic and a smaller effective mass for electrons than for holes.⁵⁶

Electrochemical Measurements

Fe-Ru, Fe, or Ru catalyst-deposited electrodes were prepared via spin-coating (MS-B100, MIKASA). A 100 μL solution—acetone solution containing $\text{Ru}(\text{acac})_3$ and/or $\text{Fe}(\text{acac})_3$ (12.5 mM), aqueous solution containing RuCl_3 and FeCl_3 (12.5 mM), or aqueous suspension of FeHCRu (12.5 mM)—was dropped onto a conductive fluorine-doped tin oxide (FTO) glass substrate, spin-coated (500 rpm for 5 s, followed by 1000 rpm for 10 s), and subsequently heated at 100–550 °C for 30 min under an Ar flow (20 mL min^{-1}). Additionally, Ru (metal)-loaded electrodes were prepared by reduction of RuO_x -loaded substrate (acac-derived, heated at 450 °C) under H_2 flow (10 mL min^{-1}) at 150 °C for 15 min.⁵⁷

Electrochemical measurements were conducted in an aqueous Na_2SO_4 (0.1 M, pH 2.5, adjusted with H_2SO_4) solution under an Ar atmosphere. The prepared working electrode, Ag/AgCl reference electrode, and Pt wire counter electrode were connected to a potentiostat (VersaSTAT 4, AMETEK), and cyclic voltammograms (CV) were recorded. In some cases, 8 mM $\text{Fe}(\text{NO}_3)_3$ or 8 mM FeCl_2 was added to the solution (pH 2.5 adjusted with H_2SO_4). To assess the electrochemically active surface area (ECSA), CV curves were obtained via cyclic voltammetry between 0.6 to 0.7 V vs. Ag/AgCl (non-Faradaic region) at scan rates of 20, 30, 40, 50, 60, 70, and 80 mV s^{-1} .

Photocatalytic Reaction

Photocatalytic reactions were performed in a Pyrex top-window cell connected to a closed-circulation gas system. The amount of evolved gases was quantified employing an online gas chromatograph (thermal conductivity detector; molecular sieve 5 Å column packing; Ar carrier gas). Photocatalyst powders (50 mg) were dispersed in 100 mL of an aqueous solution of $\text{Fe}(\text{NO}_3)_3$ (pH 2.4, adjusted with HNO_3) at a concentration of 8 mM, or in 100 mL of an aqueous of $\text{Fe}(\text{ClO}_4)_3$ and/or $\text{Fe}(\text{ClO}_4)_2$ (pH 2.4, adjusted with HClO_4) at concentrations of 4 mM each. The reaction solutions were irradiated with visible light ($\lambda > 400 \text{ nm}$) through a cutoff filter (HOYA; L42) from a 300 W Xe-arc lamp (PerkinElmer; Cermex-PE300BF). The apparent quantum efficiency (AQE) for O_2 evolution was measured using monochromatic LED light (controller (power): CL-1501; LED heads: CLH1-405-9-1-B ($\lambda = 405 \pm 8 \text{ nm}$); head top: CL-H1LCB02, Asahi Spectra Co., Ltd.). The AQE was calculated using the following equation: $\text{AQE} (\%) = (4 \times R/I) \times 100$, where R and I represent the rate of O_2 evolution and the rate of incident photons was measured using a power meter (3664 optical power meter, HIOKI E.E. CORPORATION).

Z-scheme water-splitting reactions were performed using 50 mg each of $\text{Ba}_2\text{Bi}_3\text{Nb}_2\text{O}_{11}\text{I}$ (FeHCRu -500 °C) (or $\text{Ba}_2\text{Bi}_3\text{Nb}_2\text{O}_{11}\text{I}$ (acac-450 °C)) and RuO_x -loaded $\text{SrTiO}_3\text{:Rh}$ as the O_2 - and H_2 -evolving photocatalysts, respectively. These photocatalysts were suspended in an aqueous $\text{Fe}(\text{NO}_3)_3$ solution (2 mM, 100 mL). The pH of the solution was adjusted to approximately 2.4 using a diluted aqueous HNO_3 solution. The suspension was then irradiated with visible light ($\lambda > 400 \text{ nm}$).

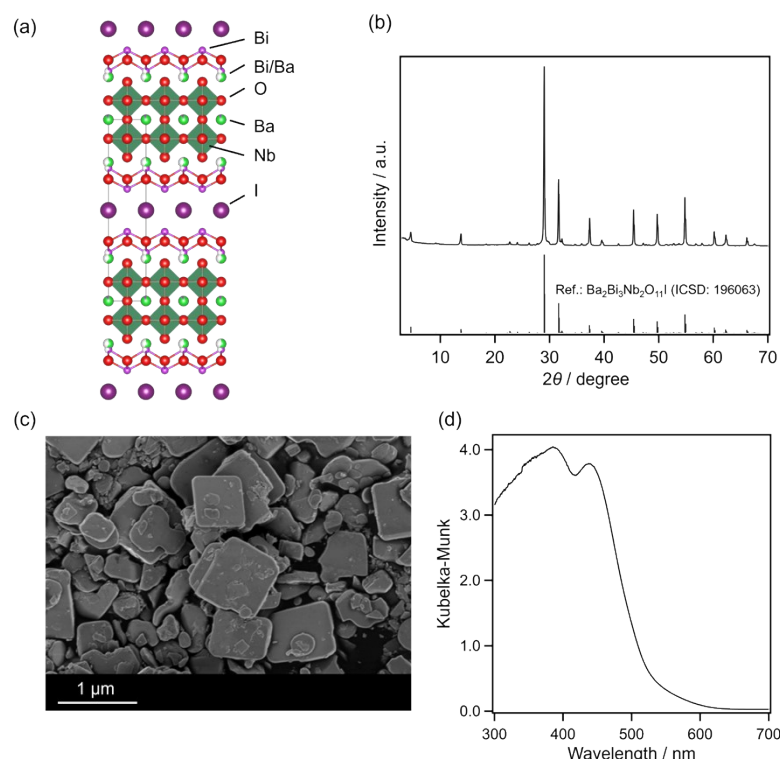


Figure S1. (a) Crystal structure, (b) XRD pattern, (c) SEM image, and (d) diffuse reflectance spectrum of $\text{Ba}_2\text{Bi}_3\text{Nb}_2\text{O}_{11}\text{I}$. XRD analysis indicates the formation of a single-phase material, and SEM observations reveal plate-like particles with an approximate size of $1\ \mu\text{m}$. The diffuse reflectance spectrum aligns well with the reported data.^{S1}

In this study, a Sillén–Aurivillius-type oxyiodide, $\text{Ba}_2\text{Bi}_3\text{Nb}_2\text{O}_{11}\text{I}$, was used as a photocatalyst. The Sillén(–Aurivillius)-type oxyhalides are recognized as promising O_2 -evolving photocatalysts in Z-scheme water splitting systems.^{S6,S8-S11} Among them, Sillén–Aurivillius oxyiodides have demonstrated superior performance compared to their chloride and bromide counterparts, owing to their long-wavelength absorption and improved charge transport properties.^{S6,S12,S13} $\text{Ba}_2\text{Bi}_3\text{Nb}_2\text{O}_{11}\text{I}$, in particular, shows the longest absorption edge (532 nm) among reported Sillén–Aurivillius oxyiodides.^{S12,S13} Based on these advantages, we selected $\text{Ba}_2\text{Bi}_3\text{Nb}_2\text{O}_{11}\text{I}$ as a model photocatalyst and attempted to further enhance its activity by optimizing the surface cocatalyst structure.

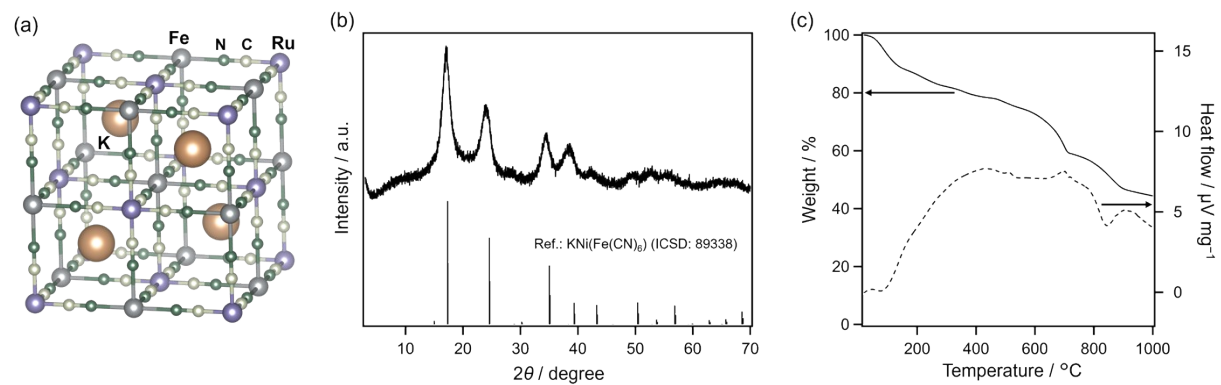


Figure S2. (a) Crystal structure, (b) XRD pattern, and (c) TG-DTA profile of iron hexacyanoruthenate ($\text{KFe}[\text{Ru}(\text{CN})_6]$, FeHCRu) under flowing nitrogen. A simulated XRD pattern of $\text{KNi}[\text{Fe}(\text{CN})_6]$, which possesses nearly identical crystal structure, is included as a reference.

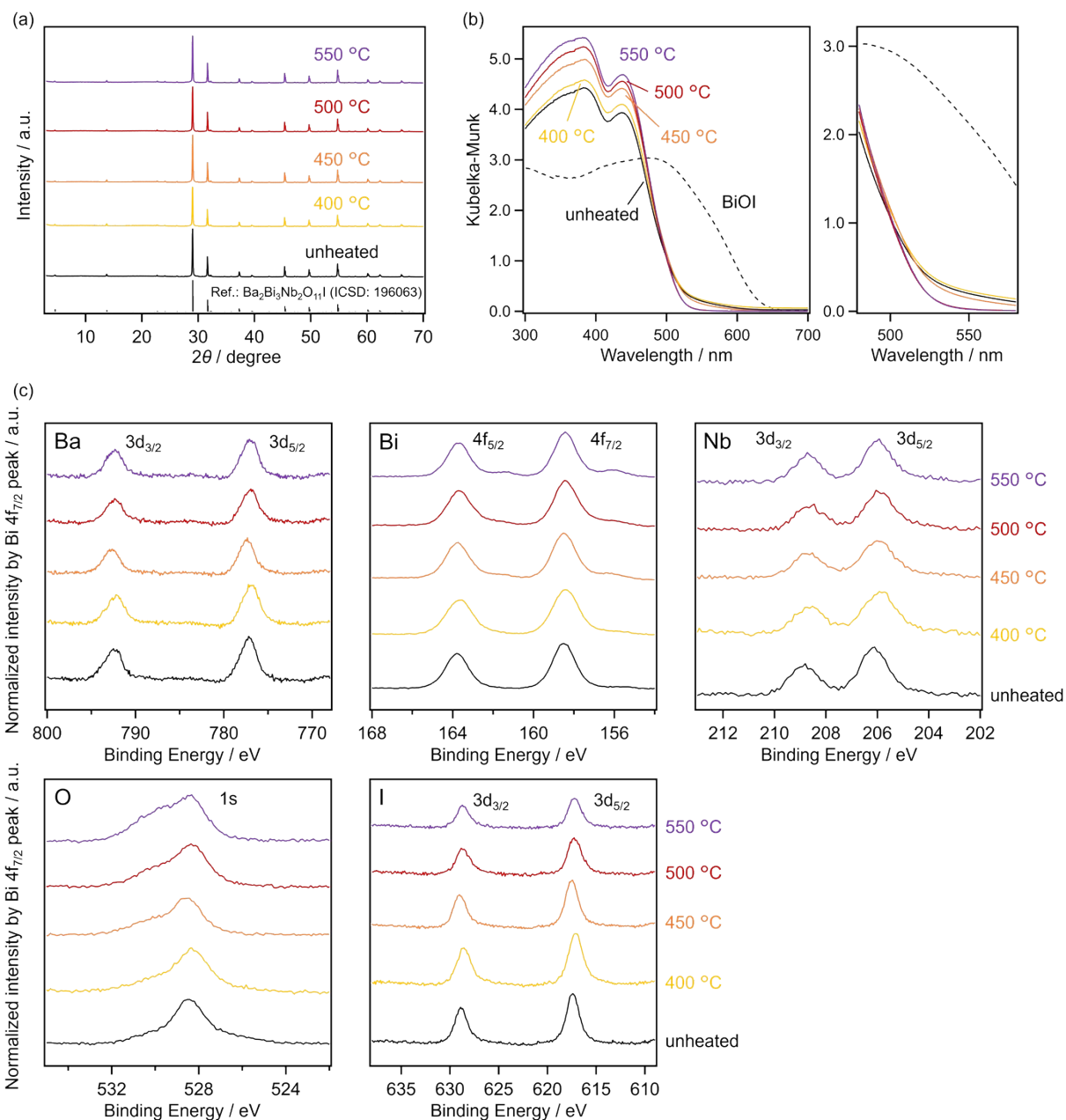


Figure S3. (a) XRD patterns, (b) diffuse reflectance spectra, and (c) XPS profiles of $\text{Ba}_2\text{Bi}_3\text{Nb}_2\text{O}_{11}$ samples heated at different temperatures under Ar flow.

Table S1. Surface Nb/Bi and I/Bi ratios of $\text{Ba}_2\text{Bi}_3\text{Nb}_2\text{O}_{11}\text{I}$ samples heated at different temperatures under Ar flow, determined by XPS analysis (Figure S3c).

	Sample				
	unheated	400 °C	450 °C	500 °C	550 °C
Nb/Bi	0.44	0.41	0.39	0.38	0.40
I/Bi	0.35	0.33	0.30	0.25	0.22

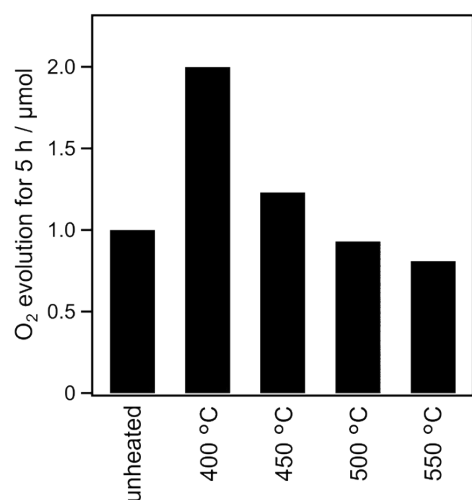


Figure S4. Amounts of O_2 evolved over 5 h reaction for $\text{Ba}_2\text{Bi}_3\text{Nb}_2\text{O}_{11}\text{I}$ samples heated at different temperatures under Ar flow in $\text{Fe}(\text{NO}_3)_3$ (aq) (8 mM) under visible light ($\lambda > 400$ nm) irradiation.

The XRD patterns of the $\text{Ba}_2\text{Bi}_3\text{Nb}_2\text{O}_{11}\text{I}$ samples remain nearly unchanged after calcination (Figure S3a), indicating that the bulk crystal structure was retained. In contrast, diffuse reflectance spectra (Figure S3b) and XPS measurements (Figure S3c and Table S1) revealed changes in the surface composition induced by calcination. It has been reported that a trace amount of BiOI, a raw material, remains on the $\text{Ba}_2\text{Bi}_3\text{Nb}_2\text{O}_{11}\text{I}$ synthesized by the flux method.^{S1} Upon calcination of this material, a decrease in the absorption attributed to BiOI (Figure S3b) and a reduction in the I/Bi atomic ratio with increasing calcination temperature (Table S1) were observed. These results indicate that the calcination process effectively removes or decomposes surface BiOI while preserving the bulk structure of $\text{Ba}_2\text{Bi}_3\text{Nb}_2\text{O}_{11}\text{I}$. Furthermore, we evaluated the impact of calcination on the O_2 evolution activity of $\text{Ba}_2\text{Bi}_3\text{Nb}_2\text{O}_{11}\text{I}$ (Figure S4). The photocatalytic O_2 evolution activity did not show a significant decrease after calcination, suggesting that the calcination does not adversely affect the intrinsic activity of the material.

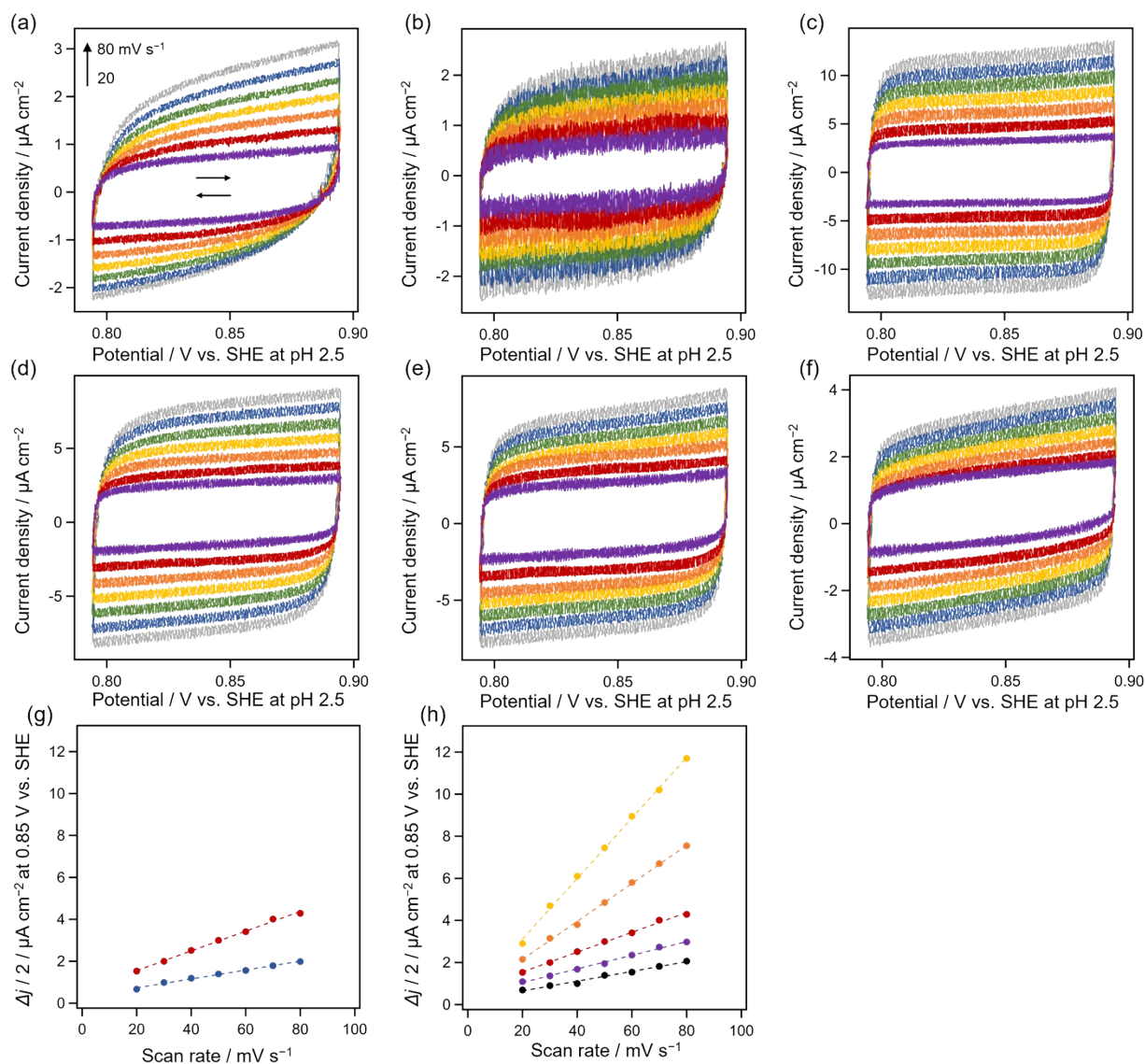


Figure S5. CV of electrodes loaded with Fe-Ru catalyst prepared using $\text{Fe}(\text{acac})_3$ and $\text{Ru}(\text{acac})_3$ (a) or FeHCRu (b-f) at temperatures of (a) 450°C , (b) 100°C , (c) 400°C , (d) 450°C , (e) 500°C , and (f) 550°C . (g) Estimation of the double-layer capacitance by plotting the current density variation against scan rates to fit a linear regression (Fe-Ru catalysts loaded using FeHCRu at 500°C in the red line ($47.1 \mu\text{F cm}^{-2}$) and using $\text{Fe}(\text{acac})_3$ and $\text{Ru}(\text{acac})_3$ at 450°C in the blue line ($21.2 \mu\text{F cm}^{-2}$)). (h) Comparison of the current density variation against scan rates for Fe-Ru catalysts loaded using FeHCRu at 100°C in black line ($23.1 \mu\text{F cm}^{-2}$), 400°C in yellow line ($144 \mu\text{F cm}^{-2}$), 450°C in orange line ($90.4 \mu\text{F cm}^{-2}$), 500°C in red line ($47.1 \mu\text{F cm}^{-2}$), and 550°C in purple line ($32.3 \mu\text{F cm}^{-2}$).

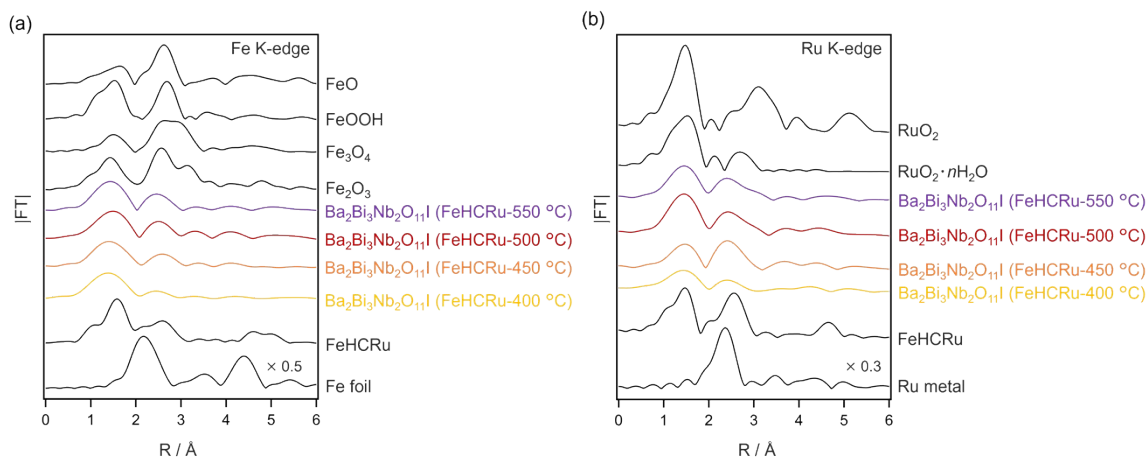


Figure S6. (a) Fe K-edge and (b) Ru K-edge Fourier-transformed extended X-ray absorption fine structure (EXAFS) for $\text{Ba}_2\text{Bi}_3\text{Nb}_2\text{O}_{11}\text{I}$ (FeHCRu- T °C) samples. The Fe K-edge EXAFS spectra revealed that the peak position of the first coordination shell in $\text{Ba}_2\text{Bi}_3\text{Nb}_2\text{O}_{11}\text{I}$ (FeHCRu- T °C) is close to the bond length of Fe–O. The Ru K-edge EXAFS spectra of $\text{Ba}_2\text{Bi}_3\text{Nb}_2\text{O}_{11}\text{I}$ (FeHCRu- T °C) appear to be a combination of those of Ru metal, (hydrus) oxide, and FeHCRu.

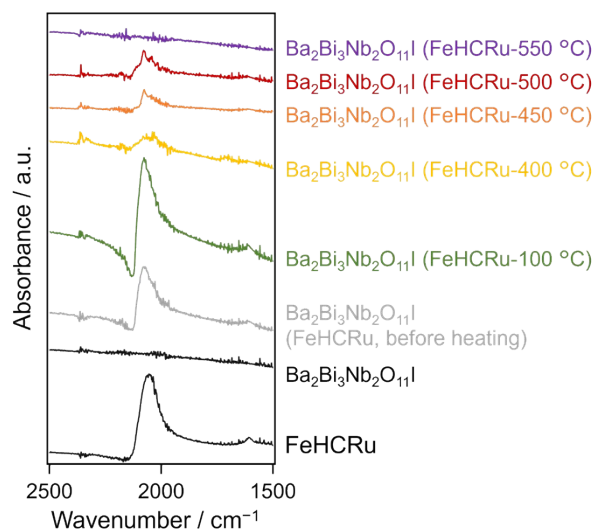


Figure S7. ATR IR spectra for the $\text{Ba}_2\text{Bi}_3\text{Nb}_2\text{O}_{11}\text{I}$ sample loaded with FeHCRu before heating and after heat treatment at 100 °C, 400 °C, 450 °C, 500 °C, and 550 °C.

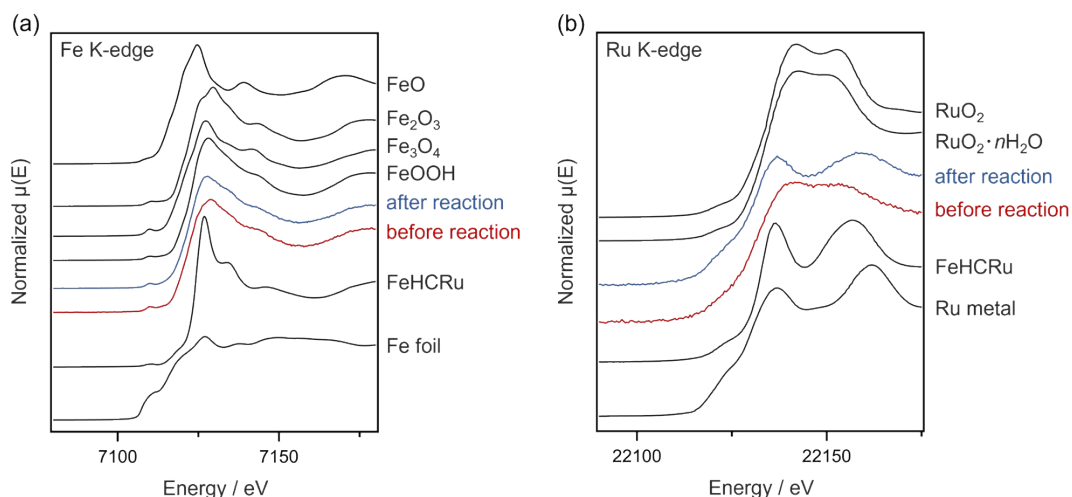


Figure S8. (a) Fe K-edge and (b) Ru K-edge XANES spectra for $\text{Ba}_2\text{Bi}_3\text{Nb}_2\text{O}_{11}$ (FeHCRu-500 °C) before and after photocatalytic water oxidation in $\text{Fe}(\text{NO}_3)_3$ (aq) (8 mM) under visible light ($\lambda > 400$ nm) irradiation.

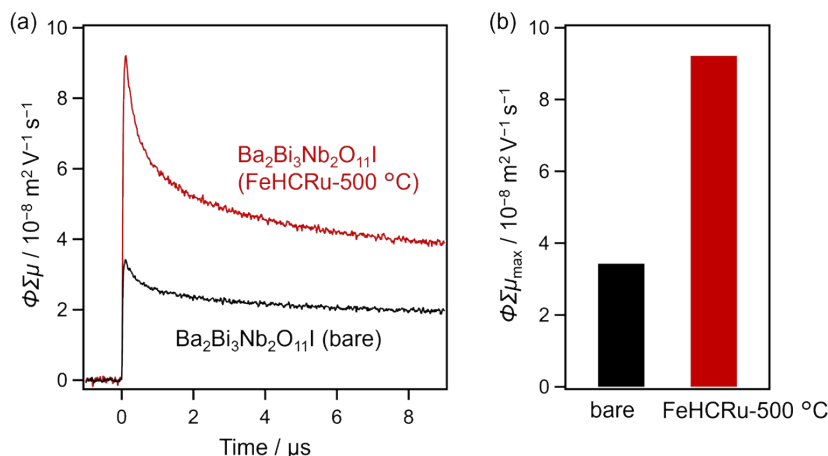


Figure S9. (a) TRMC transients and (b) TRMC transient maxima ($\phi\Sigma\mu_{\max}$) of $\text{Ba}_2\text{Bi}_3\text{Nb}_2\text{O}_{11}$ (black) and $\text{Ba}_2\text{Bi}_3\text{Nb}_2\text{O}_{11}$ (FeHCRu-500 °C) (red).

The FeHCRu-loaded sample exhibited a higher TRMC signal intensity compared to the bare sample, which can be attributed to the rapid extraction of holes by the cocatalyst within the time resolution. In addition, a relatively fast signal decay was observed, indicating electron transfer from the semiconductor to the cocatalyst. Indeed, the estimated lifetime of BBNOI (FeHCRu-500°C) ($\tau = 3.1 \mu\text{s}$) is shorter than that of bare $\text{Ba}_2\text{Bi}_3\text{Nb}_2\text{O}_{11}$ ($\tau = 30.8 \mu\text{s}$). These results suggest that FeHCRu functions as a bifunctional cocatalyst, facilitating the collection of both photoexcited electrons and holes. Such bifunctional cocatalysts may act as recombination centers for electrons and holes; therefore, for efficient photocatalysis, it is desirable to employ photocatalysts in which the oxidation and reduction sites (facets) are intrinsically separated.

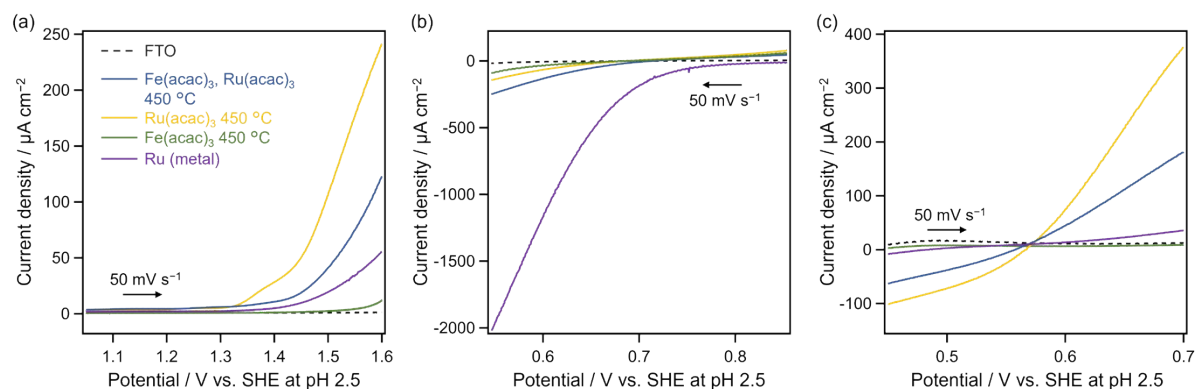


Figure S10. LSV results for electrodes prepared using acac-based precursors in aqueous Na_2SO_4 solution (a) in the absence of redox additives, (b) in the presence of Fe^{3+} electron acceptor, and (c) in the presence of Fe^{2+} electron donor. The catalytic activity for water oxidation was evaluated in (a), that for Fe^{3+} reduction in (b), and that for Fe^{2+} oxidation in (c).

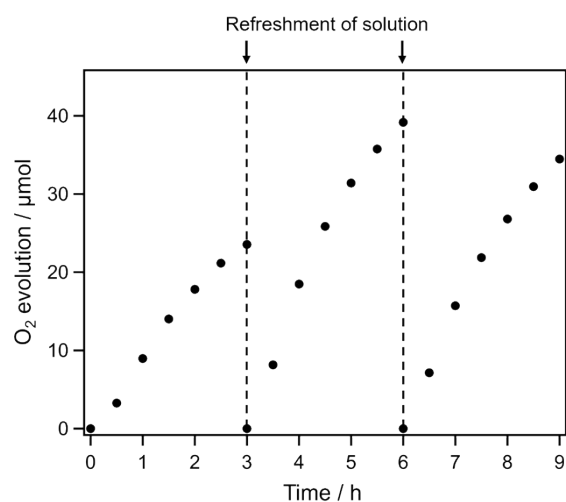


Figure S11. Repeatability test of photocatalytic O_2 evolution using $\text{Ba}_2\text{Bi}_3\text{Nb}_2\text{O}_{11}\text{l}$ (FeHCRu-500 °C) in $\text{Fe}(\text{NO}_3)_3$ (aq) (8 mM) under visible light ($\lambda > 400 \text{ nm}$) irradiation.

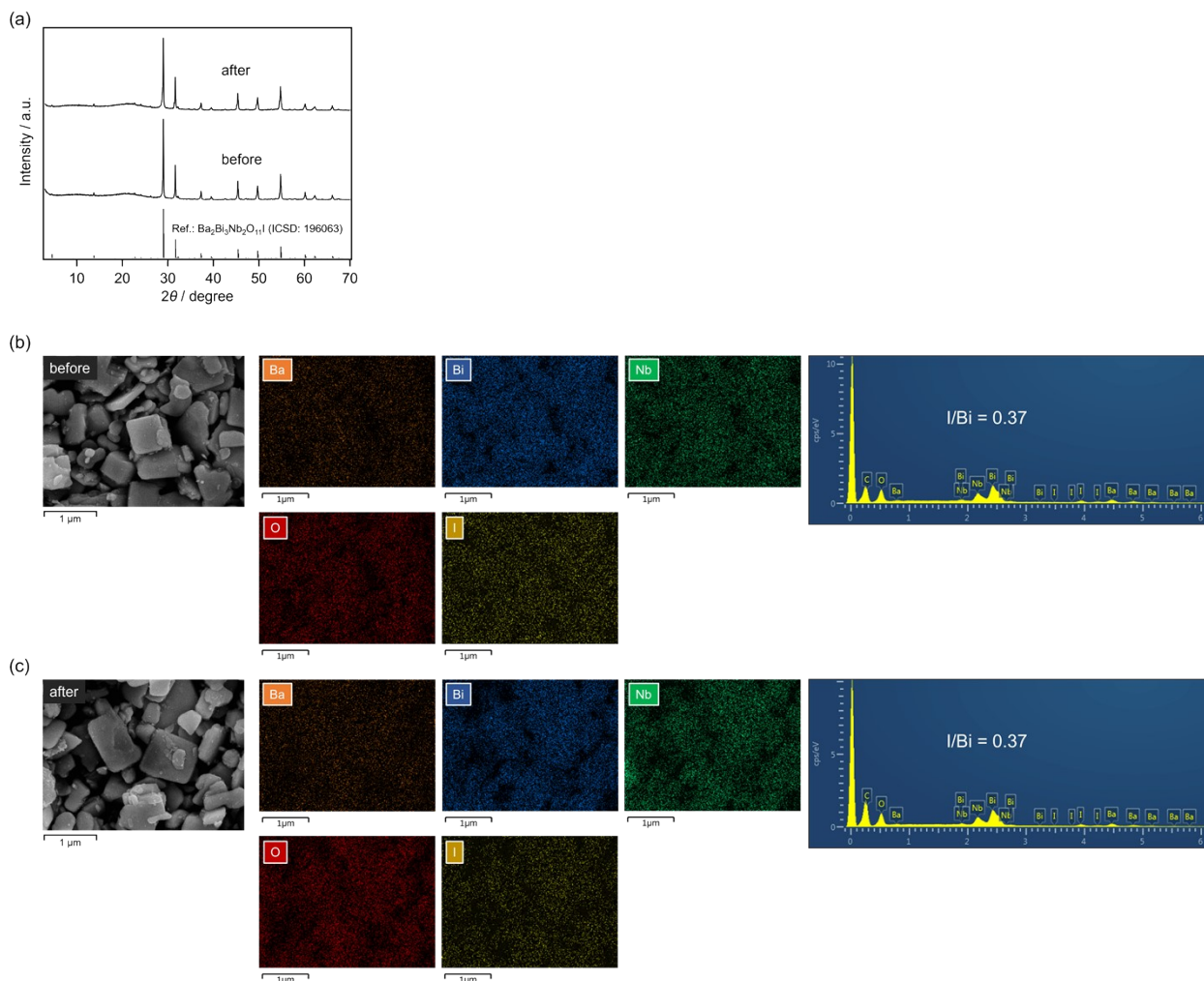


Figure S12. (a) XRD patterns, (b,c) SEM-EDX analysis of the $\text{Ba}_2\text{Bi}_3\text{Nb}_2\text{O}_{11}$ (FeHCRu-500 °C) before and after the repeatability test of photocatalytic water oxidation in $\text{Fe}(\text{NO}_3)_3$ (aq) (8 mM) under visible light irradiation (Figure S11).

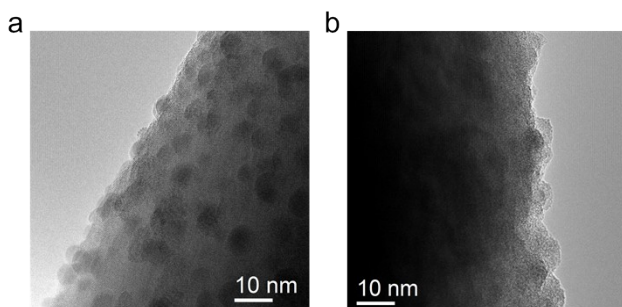


Figure S13. TEM images of $\text{Ba}_2\text{Bi}_3\text{Nb}_2\text{O}_{11}$ (FeHCRu-500 °C) (a) before and (b) after the repeatability test of photocatalytic water oxidation in $\text{Fe}(\text{NO}_3)_3$ (aq) (8 mM) under visible light irradiation (Figure S11).

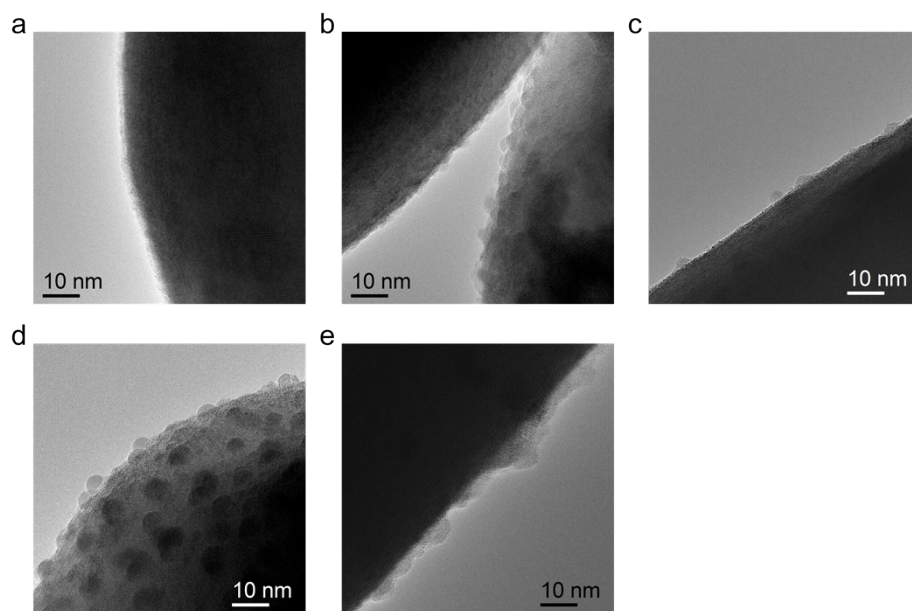


Figure S14. TEM images of bare $\text{Ba}_2\text{Bi}_3\text{Nb}_2\text{O}_{11}\text{I}$ (a) and $\text{Ba}_2\text{Bi}_3\text{Nb}_2\text{O}_{11}\text{I}$ (FeHCRu- T °C) ($T = 400$ (b), 450 (c), 500 (d), and 550 (e)).

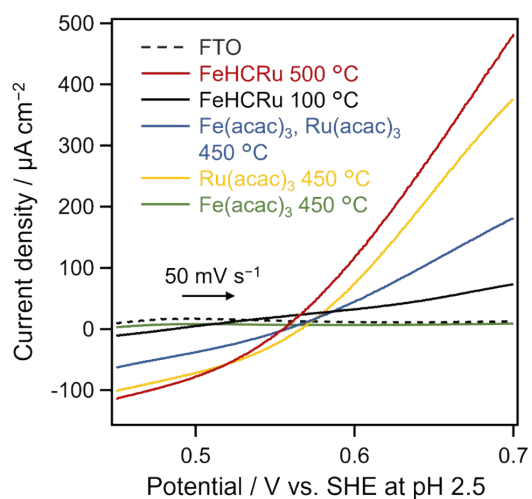


Figure S15. LSV results for various electrodes in an aqueous Na_2SO_4 solution containing an Fe^{2+} electron donor. The catalytic activity for Fe^{2+} oxidation was evaluated.

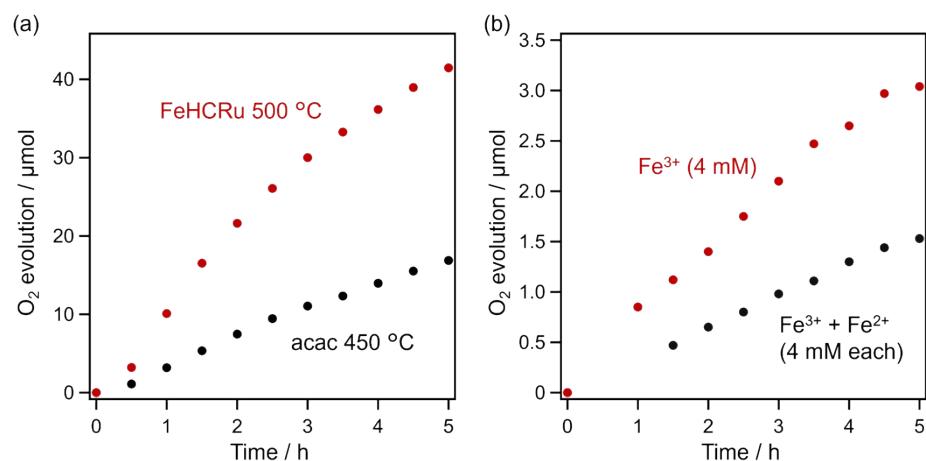


Figure S16. (a) Time course of O₂ evolution over Ba₂Bi₃Nb₂O₁₁I (FeHCRu-500 °C) and Ba₂Bi₃Nb₂O₁₁I (acac-450 °C) in Fe(NO₃)₃ (aq) (8 mM) at pH 2.4 under visible light ($\lambda > 400$ nm) irradiation. This dataset corresponds to the results presented in Figure 1. (b) Time course of O₂ evolution over Ba₂Bi₃Nb₂O₁₁I (FeHCRu-500 °C) in Fe(ClO₄)₃ (aq) (4 mM) at pH 2.4 under visible light ($\lambda > 400$ nm) irradiation, in the absence (red) and presence (black) of Fe(ClO₄)₂ (4 mM).

We examined the impact of the reverse reaction during the half-reaction in aqueous solution of Fe(NO₃)₃ (Figure S16a). As the O₂ evolution reaction proceeded, the concentration of Fe²⁺ increased, leading to the oxidation of Fe²⁺. This reverse reaction inhibited the overall reaction rate, resulting in a gradual decrease in the O₂ evolution rate. Furthermore, in the presence of both Fe²⁺ and Fe³⁺, the activity was lower than that in the Fe³⁺ system, suggesting a competitive reverse process (Figure S16b). However, in the Z-scheme system (Figure 5), the prompt oxidation of Fe²⁺ to Fe³⁺ by the H₂ evolution photocatalyst suppressed the accumulation of Fe²⁺, which enabled the steady evolution of O₂ through the reaction.

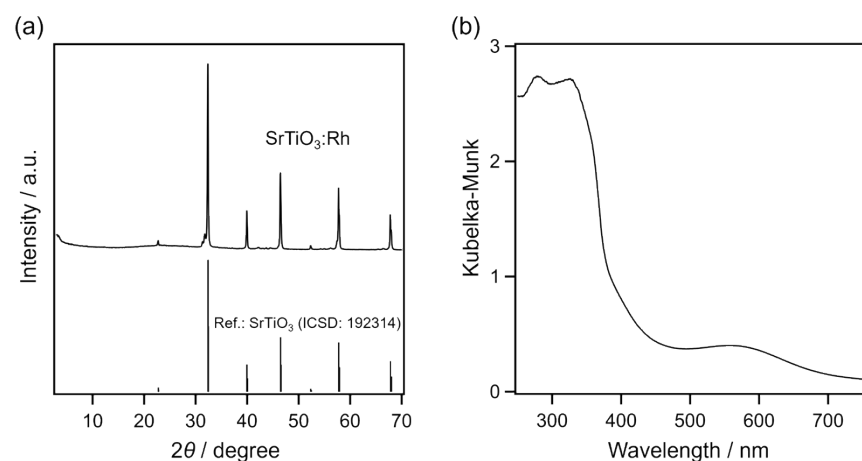


Figure S17. (a) XRD pattern and (b) diffuse reflectance spectrum of SrTiO₃:Rh.

References

- S1. R. Takahashi, M. Ogawa, H. Suzuki, O. Tomita, A. Nakada, S. Nozawa, A. Saeki and R. Abe, *Inorg. Chem.*, 2025, **64**, 9163-9171.
- S2. R. D. Shannon and R. K. Waring, *J. Phys. Chem. Solids*, 1985, **46**, 325-330.
- S3. R. Konta, T. Ishii, H. Kato and A. Kudo, *J. Phys. Chem. B*, 2004, **108**, 8992-8995.
- S4. Y. Sasaki, A. Iwase, H. Kato and A. Kudo, *J. Catal.*, 2008, **259**, 133-137.
- S5. A. Gotoh, H. Uchida, M. Ishizaki, T. Satoh, S. Kaga, S. Okamoto, M. Ohta, M. Sakamoto, T. Kawamoto, H. Tanaka, M. Tokumoto, S. Hara, H. Shiozaki, M. Yamada, M. Miyake and M. Kurihara, *Nanotechnology*, 2007, **18**, 345609.
- S6. K. Ogawa, H. Suzuki, C. Zhong, R. Sakamoto, O. Tomita, A. Saeki, H. Kageyama, and R. Abe, *J. Am. Chem. Soc.*, 2021, **143**, 8446-8453.
- S7. J. Seok, K. Y. Ryu, J. A. Lee, I. Jeong, N.-S. Lee, J. M. Baik, J. G. Kim, M. J. Ko, K. Kim, and M. H. Kim, *Phys. Chem. Chem. Phys.*, 2015, **17**, 3004-3008.
- S8. H. Fujito, H. Kunioku, D. Kato, H. Suzuki, M. Higashi, H. Kageyama and R. Abe, *J. Am. Chem. Soc.*, 2016, **138**, 2082-2085.
- S9. H. Suzuki, H. Kunioku, M. Higashi, O. Tomita, D. Kato, H. Kageyama and R. Abe, *Chem. Mater.*, 2018, **30**, 5862-5869.
- S10. H. Kunioku, M. Higashi, C. Tassel, D. Kato, O. Tomita, H. Kageyama and R. Abe, *Chem. Lett.*, 2017, **46**, 583-586.
- S11. A. Nakada, M. Higashi, T. Kimura, H. Suzuki, D. Kato, H. Okajima, T. Yamamoto, A. Saeki, H. Kageyama and R. Abe, *Chem. Mater.*, 2019, **31**, 3419-3429.
- S12. M. Ogawa, H. Suzuki, K. Ogawa, O. Tomita and R. Abe, *Solid State Sci.*, 2023, **141**, 107221.
- S13. K. Ogawa, H. Suzuki, A. Walsh and R. Abe, *Chem. Mater.*, 2023, **35**, 5532-5540.